Applied Geochemistry 168 (2024) 106027

Contents lists available at ScienceDirect

Applied Geochemistry

journal homepage: www.elsevier.com/locate/apgeochem

Influence of salt aggregate on the degradation of hybrid alkaline cement (HAC) concretes in magnesium chloride-rich saline solution simulating evaporite rock

Ricky Henning [a], Patrick Sturm [a], Sylvia Keßler [b], Gregor J.G. Gluth [a,*]

[a] 7.4 Technology of Construction Materials, Bundesanstalt für Materialforschung und -prüfung (BAM), Unter den Eichen 87, 12205, Berlin, Germany
[b] Engineering Materials and Building Preservation, Helmut-Schmidt-University/University of the Federal Armed Forces Hamburg, Friedrich-Ebert-Damm 245, 22159, Hamburg, Germany

ARTICLE INFO

Editorial handling by Erich Wieland

Keywords:
Nuclear waste repository
Evaporite rock
Magnesium chloride brine
Concrete
Salt aggregate
Hybrid alkaline cement
Degradation

ABSTRACT

Concretes produced from salt aggregate and hybrid alkaline cements, an alkali-activated slag/fly ash blend, or a Portland cement were exposed to a magnesium chloride-rich saline solution ($[Mg^{2+}]$ = 3.6 m, $[Cl^{-}]$ = 8.3 m), representing a solution formed after contact of surface water with evaporite rock (rock salt) in a nuclear waste repository. The hydration and deterioration of the concretes were studied with X-ray diffraction, thermogravimetric analysis, pH mapping and permeability measurements. The results show that calcium silicate hydrate (C-S-H) or sodium-substituted calcium aluminium silicate hydrate (C-N-A-S-H) and Friedel's salt were the major reaction products in the concretes prior to exposure to the saline solution. During exposure to the saline solution, increasing amounts of C-S-H/C-N-A-S-H dissolved, and gypsum and a secondary AFm phase formed. The durability of the concretes improved with increasing amounts of Portland clinker in the cements, due to the associated differences in permeability and chemical resistance. Nevertheless, a massive increase of permeability occurred for all concretes, likely caused by crack formation due to the formation of gypsum from anhydrite in the salt aggregate. Thus, the behavior of the concretes differed from, and was more complex than, the behavior of plain cement pastes.

1. Introduction

Several of the underground repositories that are currently used as interim storage facility or considered for final disposal of nuclear waste were previously salt mines, e.g., the Asse mine and the Morsleben repository in Germany, and thus the host rock in these repositories is an evaporite rock (Bracke, 2012; Mengel et al., 2012). The planned measures to avoid radionuclide escape from such repositories into the biosphere include the construction of sealing structures made from concrete with salt aggregate (so-called 'salt concrete') to close drifts in the mine (DBE, 2004a, 2004b, 2009; Jantschik et al., 2016). The cements that have been evaluated as regards their suitability to produce the salt concrete include magnesium oxychloride cement (Bette et al., 2017; DBE, 2004b; Dinnebier et al., 2010; Jantschik et al., 2016), low-pH cements [i.e., cements with a low fraction of Portland clinker and a high fraction of supplementary cementitious materials (SCMs) to reduce the pH of their pore solution] (DBE, 2004a, 2004b, 2009) and, more recently, hybrid alkaline cements (HAC) (Henning et al., 2023).

HAC are blends of low fractions of Portland clinker or ordinary Portland cement (OPC) and high fractions of SCMs, e.g., ground granulated blast furnace slag (GGBFS) and/or fly ash (FA), activated by an alkali salt (Garcia-Lodeiro et al., 2016; Palomo et al., 2019). Their classification as 'hybrid' derives from the fact that their chemical composition is intermediate between those of OPC and alkali-activated materials (AAM). A major advantage of HAC and low-pH cements over other cements is that they release a comparatively low amount of heat during hydration (Cau Dit Coumes et al., 2006; Codina et al., 2008; Gluth and Garel, 2021; Lothenbach et al., 2012), which decreases the risk of cracking of the salt concrete caused by restrained thermal deformations during and after hydration of the cements.

A major difference between HAC and OPC is that the major reactions products of the former are sodium-substituted calcium aluminium silicate hydrate [C-N-A-S-H, sometimes abbreviated as C-(N-)A-S-H] and sodium aluminosilicate (N-A-S-H) gel (García-Lodeiro et al., 2013;

* Corresponding author.
E-mail address: gregor.gluth@bam.de (G.J.G. Gluth).

https://doi.org/10.1016/j.apgeochem.2024.106027
Received 11 December 2023; Received in revised form 3 April 2024; Accepted 25 April 2024
Available online 30 April 2024

Garcia-Lodeiro et al., 2016; Palomo et al., 2019; Gluth and Garel, 2021; Henning et al., 2022; Etcheverry et al., 2023), while the major reaction product of OPC is calcium silicate hydrate (C-S-H) (Taylor, 1997; Richardson, 1999, 2004; Lothenbach and Nonat, 2015). The structures of C-N-A-S-H and C-S-H are related to the structure of 14 Å tobermorite, but both are poorly crystalline. While some substitution of Al for Si can occur in C-S-H, Al incorporation in C-N-A-S-H is usually much more pronounced, and incorporation of Na is significant. However, also in blended cements with high fractions of SCMs, such as low-pH cements, Al incorporation in C-S-H can be significant, which is then often referred to as C-A-S-H. Due to the differences between the availabilities of the relevant elements in the cements in which these phases occur, the Ca/(Si + Al) ratio of C-N-A-S-H is generally lower than that of C-S-H. These compositional differences between C-N-A-S-H, C-A-S-H and C-S-H are associated with structural differences [for example, longer aluminosilicate chain lengths and more cross-linking in C-N-A-S-H] as well as different solubilities (e.g., Richardson, 1999; Richardson, 2004; Puertas et al., 2011; Kulik, 2011; Myers et al., 2013; Myers et al., 2014; Richardson, 2014; Myers et al., 2015; Lothenbach and Nonat, 2015). In HAC with comparatively low Ca content, N-A-S-H gel is expected as an additional reaction product. N-A-S-H is structurally and chemically similar to Na-zeolites, with its Na/Al ratio usually around 1, while the Si/Al ratio of its aluminosilicate network can vary substantially, but it is generally X-ray amorphous (e.g., Barbosa et al., 2000; Palomo et al., 2004; Duxson et al., 2005; Fletcher et al., 2005; Walkley et al., 2018; Greiser et al., 2018).

HAC and OPC differ further as regards their secondary reaction products. For OPC, these are portlandite, Ca-Al layered double hydroxides (AFm phases), and often ettringite (Taylor, 1997). The secondary products of HAC can vary depending on their starting composition. In HAC with a significant fraction of GGBFS, usually Mg-Al layered double hydroxides (hydrotalcite-type phases) and AFm phases are found; in addition, ettringite occurs in sodium sulfate-activated HAC (Gluth and Garel, 2021; Henning et al., 2022; Etcheverry et al., 2023). For HAC based on OPC and FA only (*i.e.*, without GGBFS), ettringite is a secondary product when the activator is sodium sulfate, while crystalline product phases are generally not identified when sodium hydroxide or sodium silicate is employed as activator (Donatello et al., 2013; García-Lodeiro et al., 2013; Garcia-Lodeiro et al., 2016).

Chemical similarities between HAC and ancient Roman concrete (*opus caementitium*) structures that have survived in sea water for millennia (Jackson et al., 2013a, 2013b, 2017) have been taken to imply a high chemical resistance of HAC against attack by saline solutions (Palomo et al., 2019). The mentioned similarities include their chemical compositions, with higher alkali metal contents and lower Ca contents than for OPC, as well as the occurrence of C-N-A-S-H or C-A-S-H with a low Ca/(Si + Al) ratio and potentially Ca-substituted N-A-S-H gel or zeolites as reaction products (Palomo et al., 2019). However, the resistance of low-pH cements and HAC against chemical attack by magnesium chloride-rich saline solutions formed in contact with the evaporite rock at the Morsleben repository appears to be generally inferior to that of magnesium oxychloride cements (Henning et al., 2023; Jantschik et al., 2016), and only a few additional studies on the durability of HAC in salt solutions are available (Xue et al., 2021). Therefore, a more detailed understanding of the interaction of HAC and concretes based on these with concentrated saline solutions is required.

In a recent study (Henning et al., 2023), it was demonstrated that exposure of GGBFS/FA-based HAC to magnesium chloride-rich brine leads to the formation of gypsum, Friedel's salt, Kuzel's salt and magnesium silicate hydrate (M-S-H) in these cements. The chemical durability of the cements depended on their fraction of Portland clinker, which was explained by the presence of more portlandite in these cements, which buffered pH at ~12.5 and, thus, prevented the dissolution of major reaction products for a longer time. However, the production of salt concretes for the sealing structures involves the employment of a high fraction of salt aggregate, which itself alters the pore solution of the hardening concretes, and thus potentially alters the phase assemblage of the hydrated cements. To investigate this issue and its consequences, the present study analyzed the influence of the salt aggregate on the initial phase assemblage and the degradation of salt concretes based on two HAC, an AAM, and an OPC for comparison. The HAC/AAM concretes were produced with varying fractions of Portland clinker (0–14 wt%), GGBFS (32–38 wt%), and FA (49–58 wt%), with a constant activator (Na_2SO_4) dosage of 4 %. The salt concrete based on OPC was studied for comparison. After curing for 56 days, the specimens were immersed up to 70 days in a saline solution, representative of solutions forming in contact with evaporite rock. The phase assemblage after curing and the alteration of the phase assemblage due to exposure to the solution was studied by X-ray diffraction (XRD) and thermogravimetric analysis (TGA). The permeabilities of the salt concretes were measured to evaluate the influence of the cements and the salt aggregate on their physical properties prior to and after the exposure. The results revealed important effects of the salt aggregate, including secondary minerals (impurities) in the aggregate, on the resistance of the salt concretes.

2. Materials and methods

2.1. Materials

2.1.1. Starting materials for salt concrete production

For the preparation of the salt concretes, a Portland clinker CEM I 42.5 R (Pc), a ground granulated blast furnace slag (GGBFS), a hard coal fly ash (FA), and rock salt, used as the salt aggregate, were employed. The Pc was supplied by HeidelbergCement (Germany), the GGBFS by Cemex Eisenhüttenstadt (Germany), and the FA by BauMineral (Germany; trade name of the fly ash: EFA-Füller HP). The rock salt was obtained through the German Federal Company for Radioactive Waste Disposal (*Bundesgesellschaft für Endlagerung*, BGE) from a salt mine in the area of Teutschenthal (Geiger/GTS, Germany). The Pc was supplied as granules, which were ground for 18 s in a disk mill, and the powder was sieved afterwards (mesh width = 0.90 mm); remanent grains were ground for further 18 s and sieved again to obtain fine, cement-like powder for the concrete production. The solid activator for the HAC concretes and the AAM concrete was sodium sulfate (Na_2SO_4; analytical grade). An ordinary Portland cement (OPC), CEM I 42.5 R according to EN 197–1, supplied by Cemex Rüdersdorf (Germany), was used for the reference salt concrete. EN 197-1 specifies that CEM I contains at least 95 % Portland clinker (excluding the sulfate carrier).

The chemical compositions of the starting materials were determined by inductively coupled plasma optical emission spectroscopy (ICP-OES) after total microwave digestion. 0.4 g of the respective starting material were filled into a vessel, and a mixture of 8 mL of aqua regia and 1.5 mL of hydrofluoric acid was added to the powder. The vessel was closed and transferred into a microwave oven (MLS StarT), where the suspension/solution was heated for a total of 1 h with a maximum temperature of 240 °C. Finally, 7.5 mL of hydrobromic acid were added into the vessel to bind the unreacted hydrofluoric acid and leave a clear light-yellow solution for analysis. The ICP-OES analyses were performed on a Thermo Scientific iCAP 6000 Series device, previously calibrated with appropriate commercial standard solutions; the results are shown in Table 1.

XRD patterns of the starting materials are shown in Fig. 1. The phase abundances for Pc and FA, obtained by Rietveld quantitative phase analysis (RQPA) (Henning et al., 2022), are shown in Table 2. The Pc and the OPC contained the common Portland clinker phases, *i.e.*, alite (Ca_3SiO_5), belite (Ca_2SiO_4), aluminate ($Ca_3Al_2O_6$) and ferrite (Ca_2AlFeO_5). The OPC contained gypsum and anhydrite as sulfate carriers (setting regulators), while also the Pc contained a low amount of gypsum, likely a contamination from the cement production plant. The amorphous fraction of the FA was determined to be 56 %; quartz, mullite and hematite were identified as its crystalline components (Henning et al., 2022). The GGBFS was almost completely amorphous. XRD

Table 1
Chemical compositions[a] (in wt.%) of the starting materials.

Oxide/LOI	CaO	SiO_2	Al_2O_3	Fe_2O_3	MgO	Na_2O	K_2O	SO_3	LOI/LOD[b]
Pc	62.9	23.3	5.6	2.5	1.3	0.3	0.8	1.7	0.7
GGBFS	42.8	36.5	9.3	0.4	7.8	0.4	0.4	0.5	0.4
FA	7.6	53.0	23.3	7.9	2.3	1.1	1.1	0.9	2.0
OPC	62.7	20.8	4.5	2.0	1.8	0.3	0.8	3.3	0.3
Salt aggregate	0.5	1.7	0.0	0.0	0.3	45.5	1.1	1.1	0.1

[a] Determined by inductively coupled plasma optical emission spectroscopy (ICP-OES) after total microwave digestion with aqua regia and hydrofluoric acid. Results expressed as oxides; 'Na_2O' in salt aggregate is mainly in NaCl; 'SO_3' in GGBFS includes reduced sulfur species.
[b] LOI, loss on ignition at 1000 °C according to DIN EN 196–2 for the binder starting materials; LOD, loss on drying at 105 °C for 24 h for the salt aggregate.

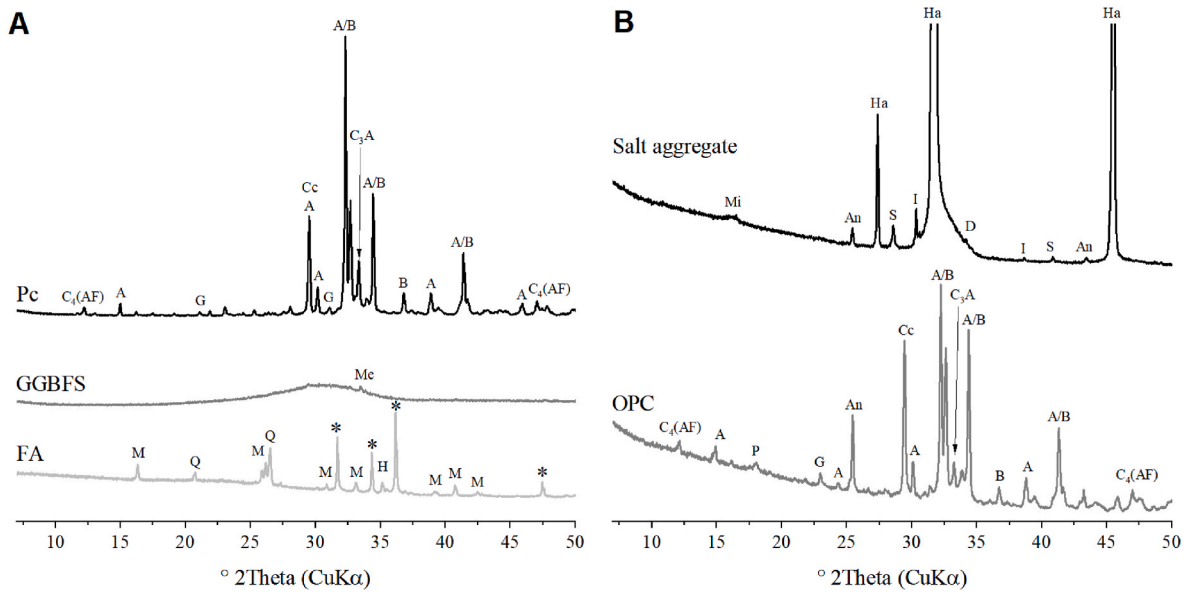

Fig. 1. XRD patterns of the starting materials: **A**, Portland clinker (Pc), ground granulated blast furnace slag (GGBFS) and fly ash (FA); and **B**, the salt aggregate and the ordinary Portland cement (OPC). Major reflections are labelled A, alite; An, anhydrite; B, belite; Cc, calcite; C_3A, aluminate; C_4AF, ferrite; D, dolomite; G, gypsum; H, hematite; Ha, halite; I, aphthitalite; M, mullite; Me, Merwinite; Mi, mirabilite; P, portlandite; Q, quartz; S, sylvite; *, zincite (internal standard).

Table 2
Phase assemblages (in wt.%) of the starting materials Pc and FA.

Phase	Pc	FA
Alite	65.0	–
Belite	16.3	–
C_3A	10.1	–
C_4AF	5.5	–
Calcite	2.4	–
Gypsum	0.4	–
Mullite	–	26.9
Quartz	–	9.1
Hematite	–	5.5
Anhydrite	–	1.4
Amorphous	–	56.2

patterns of the salt aggregate exhibited reflections of halite as the major compound, as well as minor reflections of dolomite, mirabilite, sylvite, aphthitalite and anhydrite.

The densities of the starting materials were determined by analyzing the dry powders in a Porotec Pycnomatic helium pycnometer. The densities of the Pc, the GGBFS, the FA, the sodium sulfate, and the OPC were 3.17, 2.92 (determined on a parallel batch), 2.37, 2.66, and 3.12 cm^3/g, respectively. The particle size distributions of the starting materials for HAC production were determined by laser granulometry after dispersion in isopropanol on a Sympatec HELOS/BR device. The measured median particle sizes (d_{50}) of the Pc, the GGBFS, and the FA were 15.5, 13.0 (determined on a parallel batch), and 10.2 µm

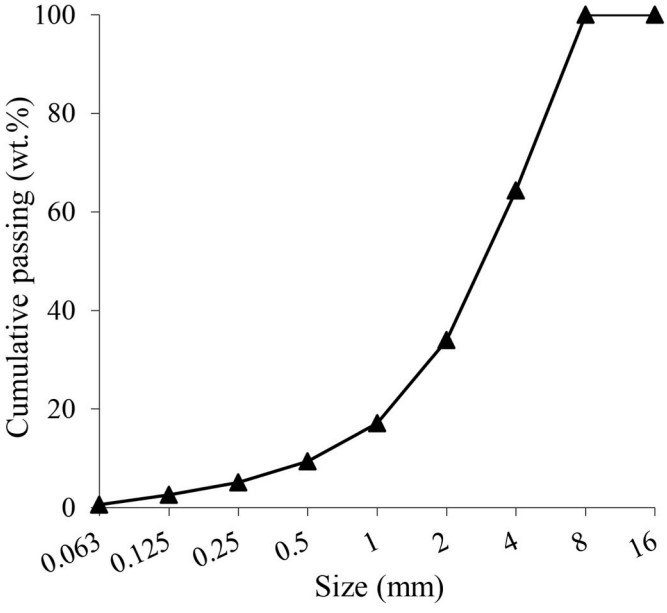

Fig. 2. Particle size distribution of the salt aggregate.

respectively. Fig. 2 shows the particle size distribution of the salt aggregate, determined by sieving in accordance with DIN EN 933–1. Since it can be expected that the salt aggregate dissolves to some extend during concrete mixing and curing, the particle size distribution determined in the dry state will not be identical to the distribution in the hardened concrete.

2.1.2. Salt concrete production

The salt concretes were produced by blending the dry binders (including the activator) with the salt aggregate at a mass ratio of 1:2. The mix designs and the designations of the binders/concretes are presented in Tables 3 and 4. In the designations of the alkali-activated GGBFS/FA blend and the HAC, C*x*S*y*, *x* refers to the approximate fraction of Pc and *y* to the fraction of sodium sulfate, respectively, in the dry mix. These dry binders were designed with increasing fractions of Pc (0–14.4 wt%) at a constant GGBFS/FA ratio of 2:3 and an activator dosage of 4 wt%, in accordance with previous studies (Henning et al., 2022, 2023). Preliminary experiments had indicated that a sodium sulfate addition of 4 wt% is the optimum dosage for HAC based on GGBFS/FA blends for a wide range of Pc contents (cf. Gluth and Garel, 2021; Henning et al., 2022). Since C0S4 does not contain Portland clinker (Pc), it is referred to as an alkali-activated GGBFS/FA blend (or simply alkali-activated material, AAM), while the alkali-activated materials with Pc, i.e., C5S4 and C14S4, are referred to as hybrid alkaline cements (HAC) throughout the text.

All salt concretes were produced by addition of deionized water at a water/binder (*w/b*) ratio of 0.35, where *b* includes all solid components of the dry binder mix (*i.e.,* OPC, Pc, GGFBS, FA, and/or sodium sulfate), to obtain workable concretes. To obtain sufficient workability for concrete OPC, it was necessary to add 1 wt% (referred to dry cement) of a commercial polycarboxylate ether (PCE)-based superplasticizer (BASF MasterGlenium SKY 591) to the concrete.

For production of the salt concretes, half of the total water content of a salt concrete was mixed for approx. 3 min with an appropriate amount of the salt aggregate (0.4 kg salt aggregate/1.0 kg water) to obtain a nearly saturated solution. All other solid compounds, including the remaining salt aggregate, were mixed in the dry state for 3 min in a rotating-pan concrete mixer (Zyklos ZK 30 HE, Permat Mischtechnik, Germany). Subsequently, the nearly-saturated solution including the undissolved aggregate was added to the solids, and the wet solids were mixed for 2 min. Finally, the remaining water was added, and the fresh concrete was mixed for additional 5 min. The resulting concrete mix designs are shown in Table 4. After mixing, the concretes were filled into molds with dimensions of 40 mm × 40 mm × 160 mm to produce the specimens for most of the subsequent experiments. The specimens for permeability testing were produced by filling the fresh concrete into cylindrical molds ($d = 50$ mm, $h = 200$ mm).

After 5 days of curing in the covered molds at laboratory temperature (~20 °C), the hardened concrete specimens were removed from the molds and further cured in a climate chamber at 23 °C/50 % relative humidity (r.H.) up to a curing age of 54 days. The cylindrical specimens for permeability testing were cut to a height of 50 mm directly after removal from the molds, i.e., at a curing age of 5 days. The prismatic specimens were cut into halves (40 mm × 40 mm × ~80 mm) at a curing age of 14 days, the cut surfaces were slightly ground (all cutting and grinding done without lubricant), and the specimens were transferred back into the climate chamber. After 54 days of curing, the specimens were immersed in a solution that was previously saturated with the salt aggregate for 2 days to saturate their pores prior to the deterioration experiments. Sound specimens for compressive strength testing and microstructural analyses without previous deterioration experiments were removed from the climate chamber after the specified curing times and dried in an oven at 40 °C for 5 days (cf. **Section 2.2**).

A schematic showing the specimen geometries during the different stages of curing, deterioration experiments and testing is provided in Fig. 3.

Table 3
Mix designs of the paste fractions of the salt concretes.

	OPC (wt. %)	Pc (wt. %)	GGBFS (wt.%)	FA (wt. %)	Na_2SO_4 (wt.%)	PCE[c] (wt.%)	*w/b*
C0S4[a]	–	–	38.4	57.6	4.0	–	0.35
C5S4[b]	–	4.8	36.5	54.7	4.0	–	0.35
C14S4[b]	–	14.4	32.6	49.0	4.0	–	0.35
OPC	99.0	–	–	–	–	1.0	0.35

[a] Referred to as alkali-activated GGBFS/FA blend, or alkali-activated material (AAM) in the present study.
[b] Referred to as hybrid alkaline cement (HAC) in the present study.
[c] PCE, polycarboxylate ether-based superplasticizer.

2.1.3. Saline solution for the deterioration experiments

For the deterioration experiments, a 'Q-Tec 4.0' saline solution, as specified by the GRS (*Gesellschaft für Anlagen-und Reaktorsicherheit*) (Henning et al., 2023) was employed. This magnesium chloride-rich salt solution, saturated with respect to halite, has been designed to represent the solutions forming in evaporite rock in contact with water (cf. Krupp, 2005), i.e., during water entry in a nuclear waste repository. A saline solution with a very similar composition has previously been used by Jantschik et al. (2016, 2018) in their study of the degradation of salt concretes based on magnesium oxychloride cement and blended cement in evaporite rock.

The Q-Tec 4.0 solution was prepared from magnesium chloride hexahydrate ($MgCl_2 \bullet 6H_2O$), magnesium sulfate heptahydrate ($MgSO_4 \bullet 7H_2O$), sodium sulfate (Na_2SO_4), potassium chloride (KCl) and sodium chloride (NaCl); all compounds were of analytical grade. Production of the solution from deionized water and the appropriate compounds followed the sequence specified by GRS (Henning et al., 2023): The water was placed in a tank, and the required amounts of salts were added in the order $MgCl_2 \bullet 6H_2O$, $MgSO_4 \bullet 7H_2O$, Na_2SO_4, KCl, ~20 % of the NaCl, remainder of the NaCl. Between the addition of each salt batch, except for the sodium sulfate, the solution was continuously stirred with a magnetic stirrer until the salt had completely dissolved, i.e., for approximately one day. After the addition of the second batch of NaCl, the solution was stirred for additional three days and then stored until required for the experiments. The mixing container was sealed during mixing and storing to avoid the evaporation of water from the solution.

The chemical composition of the resulting solution, determined by ion chromatography (Metrohm 883 Basic IC plus), is shown in Table 5. Based on this composition, the ionic strength of the solution is calculated to be 12.2 mol/kg. The pH of the solution was measured with a pH electrode, calibrated with commercial buffer solutions of pH = 4.0, 7.0, and 10.0, to be 6.2. However, at ionic strength as high as that of the Q-Tec 4.0 solution, pH measurements with electrodes yield values that can be deviant by several pH units (Altmaier et al., 2003). An expression to calculate the molal H^+ concentration (m_{H+}) in $MgCl_2$-and NaCl-rich solutions from measured pH values and the molalities of the salts has been developed by Altmaier et al. (2003). Considering only $MgCl_2$ and NaCl in solution (i.e., ignoring the lower concentrations of K^+, SO_4^{2-}, and remaining Cl^-), this approach yields $-\log(m_{H+}) = 7.9$ for the Q-Tec 4.0 solution.

2.2. Deterioration experiments

A total of 20 prismatic specimens for each salt concrete was transferred into a container ($l = 41$ cm, $w = 27$ cm, $h = 20$ cm), which was filled with 6.4 dm^3 of Q-Tec 4.0 solution and covered with a glass plate. The volume of the solution was chosen to adjust the level of solution to approx. 1 cm above the top surface of the concrete specimens. The ratio of the volume of the solution to the volume of concrete was thus generally 6400 $cm^3/(20 \times 128\ cm^3) = 2.50$. When three cylinders for

Table 4
Mix designs of the salt concretes.

Concrete designation	OPC (kg/m^3)	Pc (kg/m^3)	GGBFS (kg/m^3)	FA (kg/m^3)	Na_2SO_4 (kg/m^3)	PCE[a] (kg/m^3)	Water (kg/m^3)	Salt aggregate (kg/m^3)
C0S4	–	–	231.2	346.8	24.1	–	210.7	1204
C5S4	–	29.0	220.1	330.1	24.1	–	211.2	1207
C14S4	–	87.3	197.8	296.7	24.2	–	212.1	1212
OPC	624.4	–	–	–	–	6.2	218.5	1249

[a] PCE, polycarboxylate ether-based superplasticizer.

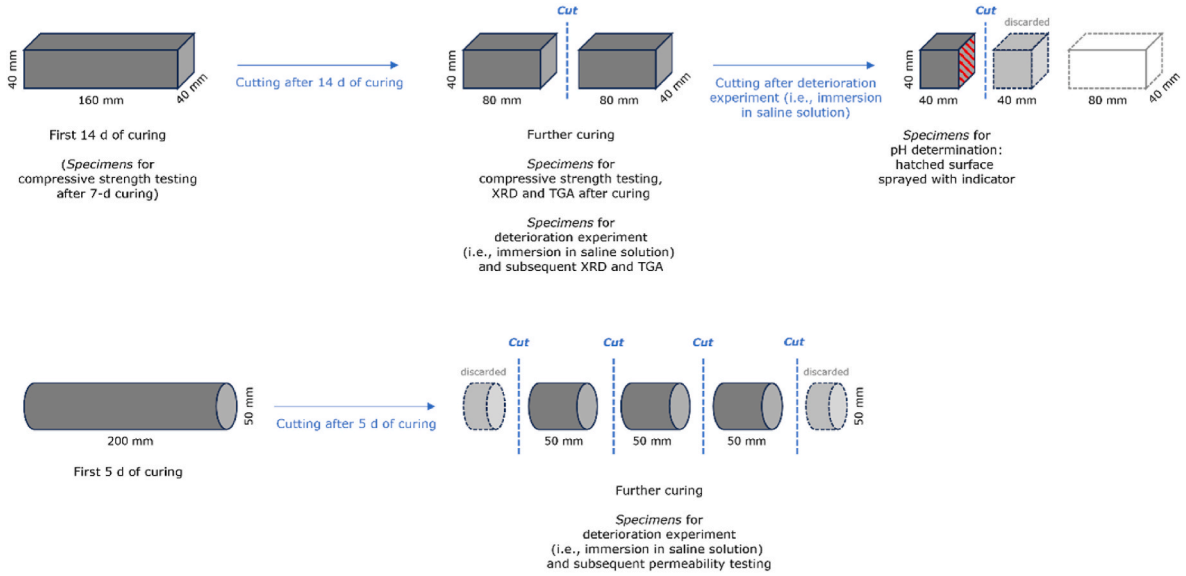

Fig. 3. Schematic of specimen geometries during curing and the subsequent experiments (see main text for details).

Table 5
Chemical composition of the Q-Tec 4.0 solution.

	Molality (mol/kg)
Na^+	0.36
K^+	0.39
Mg^{2+}	3.58
Cl^-	8.25
SO_4^{2-}	0.26

permeability measurements were immersed in the same container, the solution/concrete volume ratio was 6400 cm^3/(20 × 128 cm^3 + 3 × 98.2 cm^3) = 2.24. The solution was neither stirred nor exchanged during the experiments.

After 7, 28, 56 and 70 days of exposure, respectively, four concrete specimens per mix design were removed from the saline solution and dried in an oven at 40 °C for 5 days, after which they were submitted to microstructural analyses or permeability testing. Oven-drying was chosen to enable complete drying of the salt concretes while minimizing alteration of the deterioration front due to transport/dissolution of ions in ethanol or isopropanol (if organic solvent drying had been used). The drying temperature was chosen to be low to avoid extensive microstructural damage: Contrary to oven-drying at 105 °C, drying of cementitious materials at temperatures below 40–60 °C can be assumed to cause only minor deterioration of hydrate phases (Collier et al., 2008). However, partial desiccation of particularly susceptible phases cannot be excluded, which was considered in the evaluation of the microstructural analyses. In addition, oven-drying of the specimens will lead to precipitation of phases in the pore space of the specimens, corresponding to the dissolved species in the pore solution.

2.3. Testing and analytical methods

2.3.1. Compressive strength testing

Compressive strength testing of the salt concretes after 7, 28 and 56 days of curing was performed on a ToniPRAX device (Toni Technik Baustoffprüfsysteme, Germany) with a loading rate of 2400 N/s. For each strength data point, three replicates were tested, and the average and standard deviation will be reported below.

2.3.2. X-ray diffraction analysis

For X-ray diffraction (XRD) analyses, the dried salt concrete specimens were manually crushed and ground to a fine powder with mortar and pestle (agate). As entire specimens were prepared in this manner, the obtained results represent an average of the deteriorated and non-deteriorated regions of the specimens after exposure to the Q-Tec 4.0 solution. The obtained powders were filled into XRD sample holders by side loading to minimize preferred orientation effects. XRD measurements were performed with an Ultima IV device (Rigaku, Japan) using Cu Kα radiation (λ = 1.5419 Å) in Bragg–Brentano geometry. The parameters for the XRD measurements were set to: cathode at 40 kV/40 mA, 0.5°/10 mm divergence slit, scanning range 5–65 °2θ, sampling interval 0.02 °2θ, and scanning speed 0.5 °2θ/min. The detector was a strip detector (D/Tex Ultra) with 5°-Soller slits.

2.3.3. Thermogravimetric analysis

Powders as prepared for the XRD analyses were used for the thermogravimetric analyses (TGA). Sample masses of 10 mg were employed. The analyses were performed with a Netzsch STA 449 C Jupiter device under flowing nitrogen gas at a heating rate of 10 K min^{-1}, starting at 40 °C and ending at 700 °C to avoid melting of halite. From the TGA curves, derivative thermogravimetry (DTG) curves were computed. The abundances of key phases were calculated from step heights in the TGA

curves and the stoichiometry of the corresponding decomposition reactions; the results are referred to 100 g of cement paste (i.e., solid binder components plus mixing water) excluding the salt aggregate, to allow comparison with results for cement pastes. Although the low maximum temperature does not allow observation of the decomposition of the sulfate anion at ~800 °C, the loss of water from gypsum at ~130 °C is sufficient to identify and quantify that phase in the TGA/DTG curves (Henning et al., 2023).

2.3.4. Estimation of deterioration depth

After exposure to the Q-Tec 4.0 solution and drying at 40 °C, as described above, one specimen per concrete mix design was cut (without lubricant) into two halves to expose surfaces (40 mm × 40 mm) for pH analyses (Fig. 3). One of the exposed surfaces was sprayed with a universal indicator solution (Unisol 410; Macherey-Nagel, Germany) and photographed 15 min after spraying. The Unisol 410 solution assumes different colors in specific nominal pH ranges, as listed in Table 6. It is noted that the colors refer to application of the indicator in solutions, i.e., the correspondence between pH and color is not necessarily accurate for sprayed surfaces; however, different coloring of different regions of the surfaces serves at least to discriminate heavily deteriorated from essentially unaffected regions.

2.3.5. Gas permeability measurements

The gas permeability of the salt concretes was determined in accordance with the RILEM/Cembureau method (RILEM TC 116-PCD, 1999) on cylinders (d = 50 mm, h = 50 mm), except that argon instead of nitrogen was used as the permeating fluid. However, given that both gases can be assumed to be inert, and considering that the dynamic viscosity of the permeating gas is included in the calculation of the permeability (eq. (1)), it follows that both gases will yield identical values for permeability.

Prior to the measurements the concretes were dried in an oven at 40 °C until constant mass ($\Delta m < 0.1$ wt% within 24 h) was reached. Afterwards, the lateral surface of the cylinders was covered with a polytetrafluoroethylene (Teflon) foil to ensure flow of the permeating fluid only through the top and bottom of the sample. The specimens were then installed in the measuring device, where they were tightened with a rubber pipe inflated to a pressure of approx. 10 bar and exposed to three different inlet pressures (P_i = 1.5, 2.0, and 3.0 bar). Each level of pressure was maintained until a steady flow was registered, which allowed the determination of the permeability according to

$$K_i = \frac{2 \bullet P_a \bullet Q_i \bullet h \bullet \mu}{A \bullet (P_i^2 - P_a^2)} \quad \text{eq. 1}$$

where P_a (Pa) and P_i (Pa) refer to atmospheric pressure at the outlet and the applied level of inlet pressure, respectively. Q_i (m^3/s) is the measured gas flow through the specimen. H (m) and A (m^2) are the height and the cross-sectional area of the specimen, respectively, and μ (Pa•s) is the dynamic viscosity of the permeating fluid.

Measurements at three different inlet pressures allows to check for leakages (RILEM TC 116-PCD, 1999), which were not observed in the present tests. The permeabilities reported below were determined as the average of the results obtained at the three inlet pressures.

Table 6
PH values and associated colors for the universal pH indicator solution (Unisol 410).

Nominal pH	Color
4	Pink
5	Orange
6	Yellow
7	Green
8	Turquoise
9	Blue
10	Purple

3. Results

3.1. Compressive strength

The compressive strengths of the salt concretes after 7, 28 and 56 days of curing are shown in Fig. 4. The early compressive strength (7 days) was similar and comparatively low (3.9−4.7 MPa) for the salt concretes C0S4, C5S4 and C14S4. This was unexpected, since an increasing Portland clinker content in HAC is usually associated with an increased early compressive strength (Gluth and Garel, 2021; Henning et al., 2022; Nath and Sarker, 2015; Park et al., 2022). Consequently, the incorporation of the salt aggregate seems to have an influence on the early hydration of the salt concretes with Pc contents in the range 0–14.4 wt%, leading to convergence of their behavior. At later curing times, the expected trend of higher compressive strength with increasing Pc content of the HAC concretes could be observed. The highest strength after 56 days was exhibited by OPC; however, while the strengths of this concrete levelled off in the period 28–56 days, the strength evolution of the HAC concretes appeared to continue after 56 days of curing.

3.2. X-ray diffraction

XRD patterns of the salt concretes after curing and after increasing durations of exposure to the solution are shown in Fig. 5. The initial phase assemblages of the salt concretes C0S4, C5S4 and C14S4 were virtually identical. Poorly crystalline C-N-A-S-H [structure related to C-S-H(I), PDF# 00-034-0002] was identified through its characteristic peak at 29.4° 2θ; this phase is generally a major reaction product of GGBFS-containing AAMs and HAC (García-Lodeiro et al., 2013; Bernal, 2016; Myers et al., 2017; Palomo et al., 2019; Gluth and Garel, 2021; Henning et al., 2022; Etcheverry et al., 2023). Reflections of the Cl^--containing AFm phase Friedel's salt (PDF# 01-078-1219) were found at 11.2° 2θ, whose formation implies an impact of the salt aggregate on the hydration of the binder. The presence of quartz (PDF# 00-046-1045), mullite (PDF# 00-015-0776) and hematite (PDF# 00-033-0664) is attributed to the FA, employed in C0S4, C5S4 and

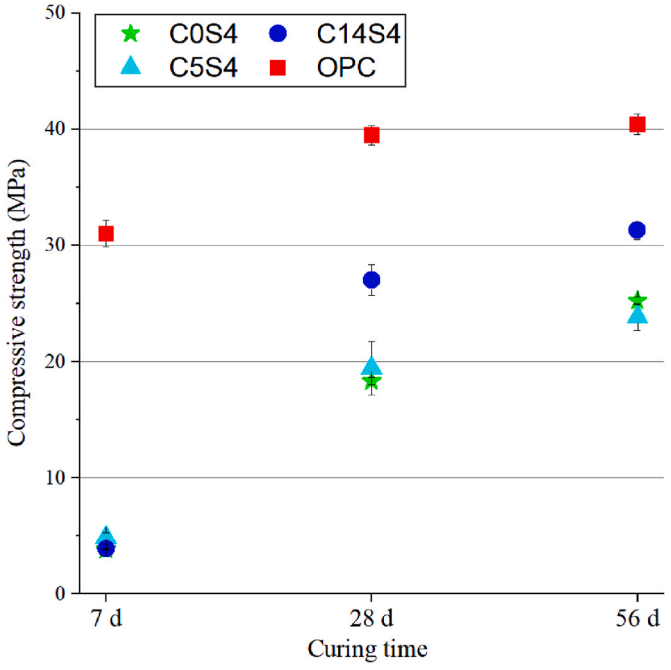

Fig. 4. Compressive strengths of the salt concretes after 7, 28 and 56 days of curing at 23 °C/50 r.H.

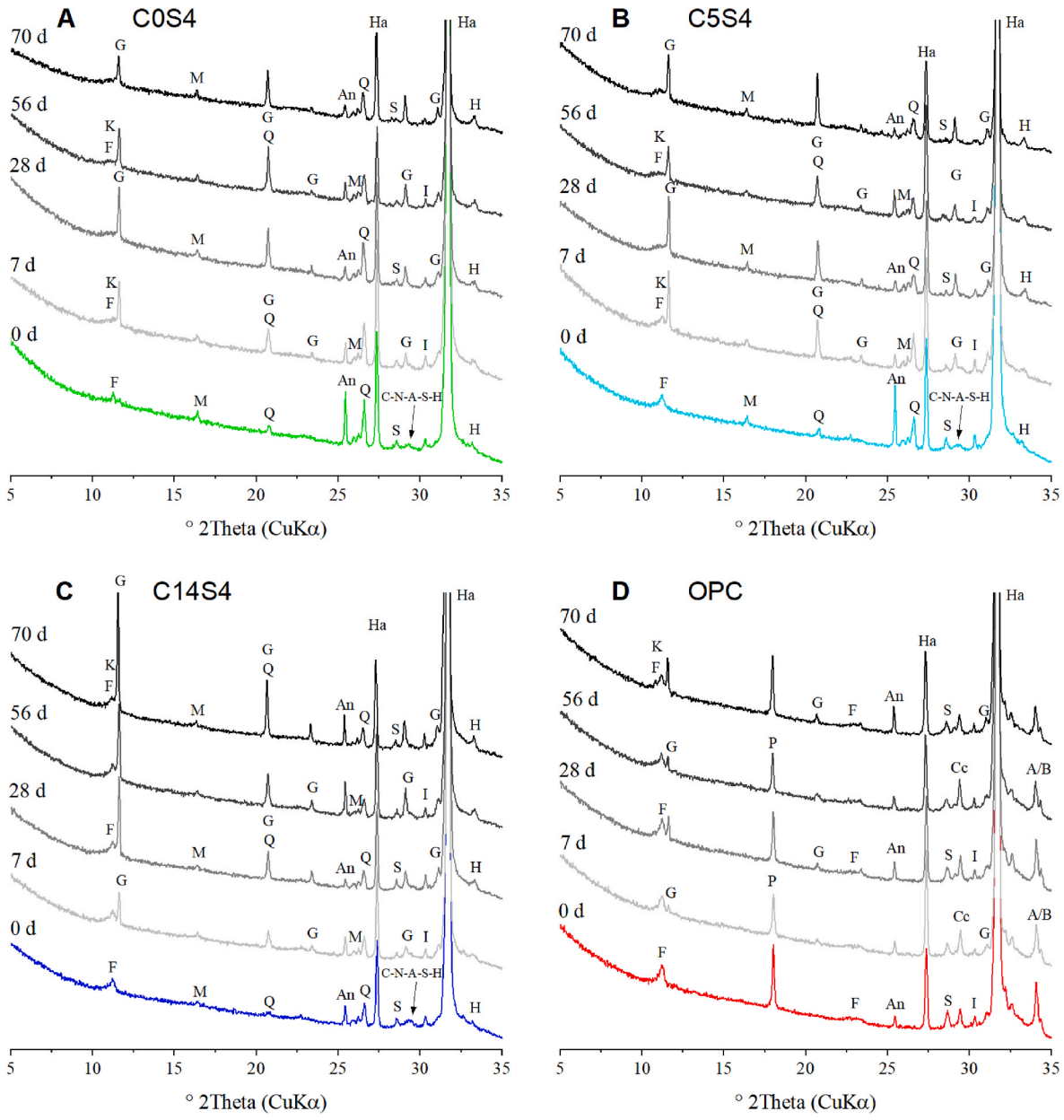

Fig. 5. XRD patterns of the salt conretes **A**, C0S4; **B**, C5S4; **C**, C14S4; and **D**, OPC, as-cured and after 7, 28, 56, and 70 days of exposure to the Q-Tec 4.0 solution. Major reflections are labelled A, alite; An, anhydrite; B, belite; Cc, calcite; C-N-A-S-H, C-N-A-S-H; F, Friedel's salt; G, gypsum; H, hematite; Ha, halite; I, aphthitalite; K, Kuzel's salt or hemicarboaluminate–Friedel's salt solid solution; M, mullite; P, portlandite; Q, quartz; S, sylvite.

C14S4. The XRD pattern of the OPC salt concrete exhibited signals of calcite (PDF# 00-005-0586), Friedel's salt, portlandite (PDF# 00-044-1481) and residual alite (PDF# 00-049-0442) and belite (PDF# 00-033-0302). Due to the incorporation of the salt aggregate, reflections of halite (PDF# 00-005-0628), anhydrite (PDF# 00-037-1496), sylvite (PDF# 01-073-0380) and aphthitalite (PDF# 01-074-1742) were found in the XRD patterns of all salt concretes.

After increasing durations of exposure to the Q-Tec 4.0 solution, alterations of the phase assemblage of the salt concretes, *i.e.*, formation of gypsum and possibly Kuzel's salt as well as dissolution of C-N-A-S-H and anhydrite, were observed. The formation of gypsum (PDF# 00-033-0311) is evidenced by the reflections at 11.6°, 20.72° and 29.11° 2θ, first notable in the salt concretes after 7 days of exposure. The increase of the intensities of these reflections with exposure time indicates that the gypsum content increased during the exposure (cf. the peak at 11.6° 2θ); the XRD patterns further suggest that the OPC salt concrete had a lower gypsum content than the other salt concretes.

The formation of Kuzel's salt (PDF# 00-019-0203; AFm phase containing Cl^- and SO_4^{2-}) in the salt concretes was suggested in the XRD patterns by the appearance of a broad reflection or shoulder in the range 10.6–11.2° 2θ, i.e., a second signal close to the main peak of Friedel's salt. Since Kuzel's salt is an intermediate in the formation of monosulfoaluminate (SO_4^{2-}-containing AFm phase) from Friedel's salt (Glasser et al., 1999; Balonis et al., 2010), it can be assumed that it formed due to the penetration of the Q-Tec 4.0 solution, which contains sulfate, into the salt concretes. However, hemicarboaluminate (PDF# 00-041-0221; AFm phase containing CO_3^{2-} and OH^-), or a solid solution between hemicarboaluminate and Friedel's salt (AFm phase containing CO_3^{2-}, OH^- and Cl^-) (Georget et al., 2022; Wilson et al., 2022), exhibits its basal reflection in same angle range, and its formation could have occurred due to slight carbonation of the samples during exposure and handling. However, a trend of delayed formation of the secondary AFm

phase with increasing Pc content was observed: The corresponding shoulder/peak can be identified after 7 days of exposure in C0S4 and C5S4, while it is notable only after 70 days in C14S4 and OPC. If carbonation during sample handling was the cause for the formation for the secondary AFm phase, one would not expect it to vary systematically with Pc content and exposure duration; thus, it appears more likely that the secondary AFm phase was Kuzel's salt.

On this basis, the delayed formation of the secondary AFm phase indicates a higher resistance of C14S4 and OPC, compared to C5S4 and C0S4, against the saline solution. In good agreement with a higher resistance of the former concretes, signals assigned to C-N-A-S-H (cf. the reflection at 29.4° 2θ) can be identified after 70 days of exposure in C14S4, while reflections of C-N-A-S-H were essentially absent in the XRD patterns of C0S4 and C5S4 already after 7 days of exposure.

It is further noted that a significant decrease of the intensities of the reflections of anhydrite (cf. the peak at 25.44° 2θ) was observed in the XRD patterns of C0S4 and C5S4 on going from as-cured to 7 days of exposure, and afterwards the intensities of these signals remained approximately constant. This implies a partial dissolution or hydration of anhydrite in the salt aggregate as a result of the exposure to the saline solution, which could have contributed to the formation of gypsum and Kuzel's salt in these salt concretes.

3.3. Thermogravimetric analysis

The TGA/DTG curves of the as-cured salt concretes and after

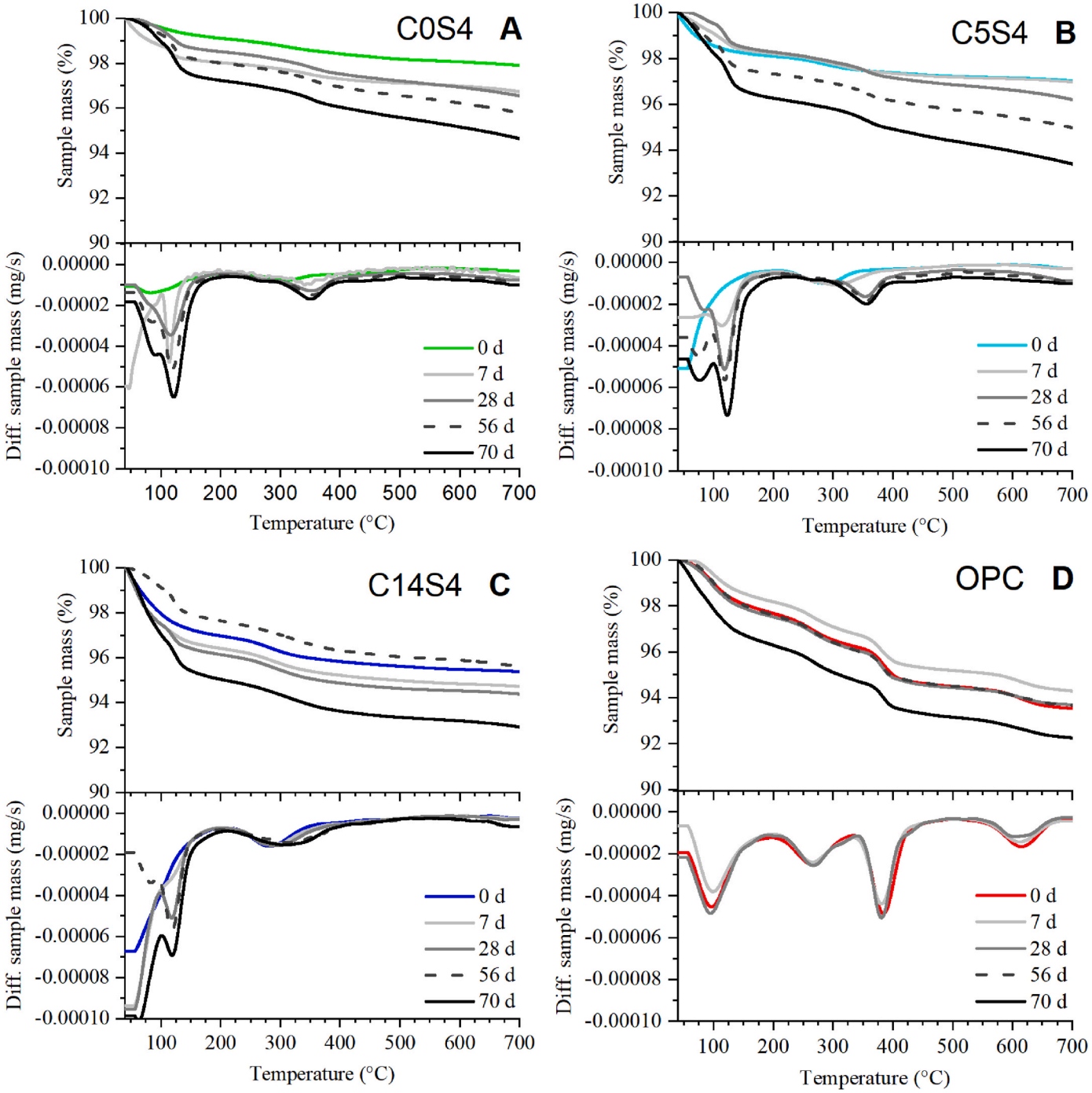

Fig. 6. TGA/DTG curves of the salt concretes **A**, C0S4; **B**, C5S4; **C**, C14S4; and **D**, OPC, as-cured and after 7, 28, 56 and 70 days of exposure to the Q-Tec 4.0 solution.

increasing durations of exposure are shown in Fig. 6. The DTG curves of the as-cured salt concretes based on HAC and the alkali-activated GGBFS/FA blend were similar, with a signal in the range 50–150 °C followed by a signal centered around 300 °C. The signal in the range 50–150 °C can be assigned to the decomposition of C-N-A-S-H, AFm phases, and N-A-S-H (Henning et al., 2022; Lothenbach et al., 2016). Except for N-A-S-H, which is amorphous, these phases were also identified by XRD as hydration products of the salt concretes. Since these phases loose interlayer water and interstitial water very easily, and thus are particularly prone to drying damage, this signal does not lend itself to quantification. The signal at around 300 °C is associated with the decomposition of AFm phases and hydrotalcite/meixnerite-type layered double hydroxides (LDH) (Henning et al., 2022; Lothenbach et al., 2016). Since hydrotalcite/meixnerite-type LDH phases were not identified in the XRD patterns of the salt concretes, this signal can be assigned to Friedel's salt and employed for its quantification. The content of Friedel's salt in the as-cured salt concretes increased with increasing fraction of Portland clinker (Fig. 7B), which can be explained by the fact that Portland clinker provides aluminate for its formation.

The DTG curves of the as-cured OPC salt concrete exhibited two additional signals at 350−420 °C and at ~590 °C. The first signal is caused by the decomposition of portlandite (Lothenbach et al., 2016), and the signal around 590 °C is attributed to the decarbonation of one or more polymorphs of $CaCO_3$ (calcite, vaterite, aragonite) (Lothenbach et al., 2016; Thiery et al., 2007). In hydrated OPC, usually calcite is the polymorph present. From their respective step heights in the TGA curves, the amounts of portlandite and calcite in the OPC salt concrete were determined to be 18 g/100 g cement paste and 5.3 g/100 g cement paste, respectively; portlandite and calcite were not detected in the HAC and alkali-activated GGBFS/FA salt concretes (Fig. 7C and D).

After increasing durations of exposure, significant changes were observed for the TGA/DTG curves of the salt concretes (Fig. 6). The total weight loss increased with increasing duration of exposure, which was mainly caused by an increased weight loss at temperatures below 100 °C. This was likely related to the mild drying conditions (5 days at 40 °C) before TGA, which could have been insufficient to remove all pore water and surface water particularly after exposure of the concretes to the highly viscous saline solution, which would also precipitate highly hygroscopic salts on evaporation. Thus, the increase of the signal at below 100 °C is likely not quantitatively related to changes of the phase

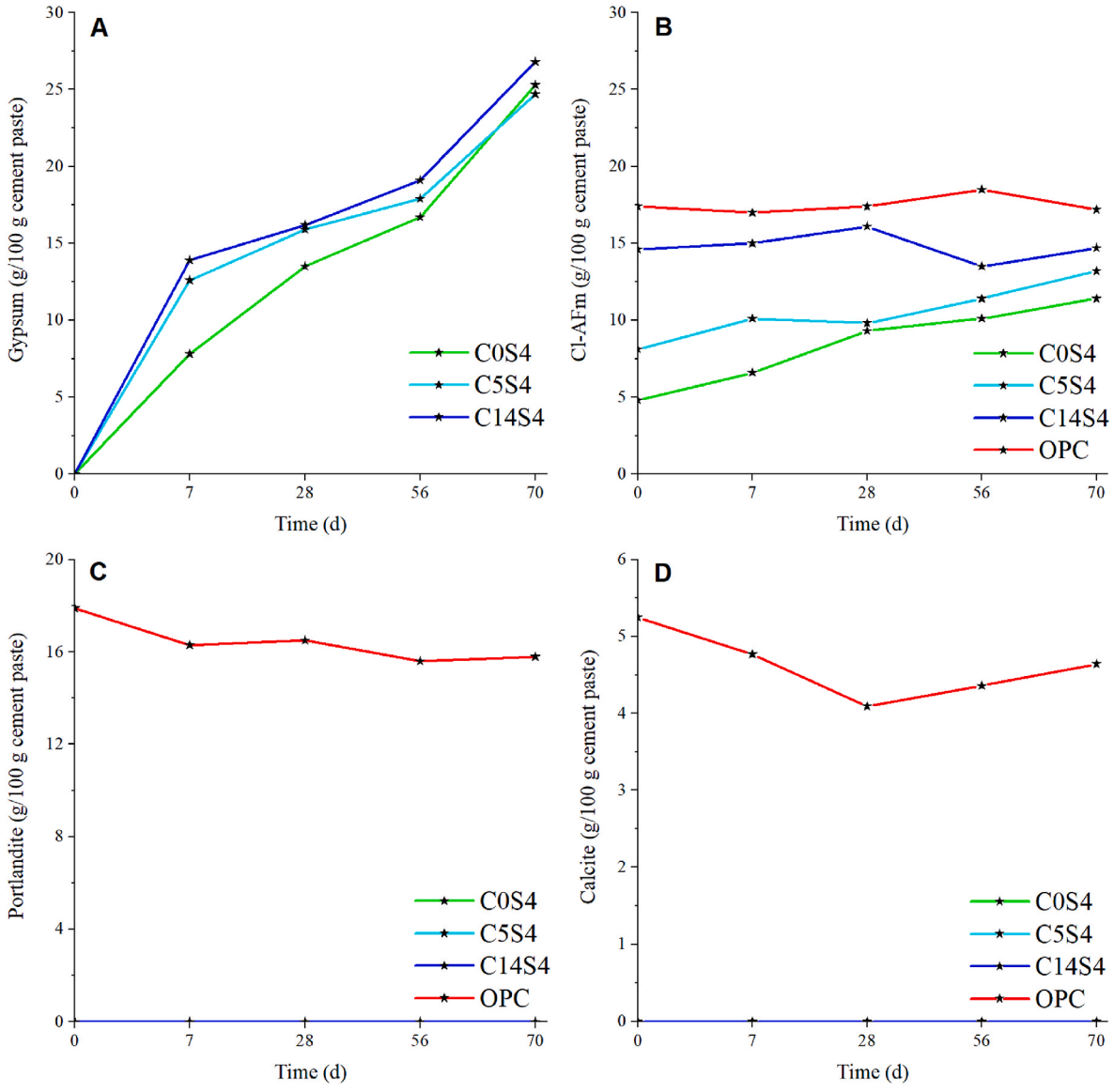

Fig. 7. Contents of **A**, gypsum; **B**, Cl-AFm; **C**, portlandite; and **D**, calcite of the salt concretes, as-cured and after 7, 28, 56 and 70 days of exposure to the Q-Tec 4.0 solution, as determined by TGA. The gypsum content of salt concrete OPC was low and could not be quantified (see text).

assemblages of the concretes.

An additional change associated with the exposure to the Q-Tec 4.0 solution was the formation of a signal centered at 130 °C in C0S4, C5S4 and C14S4. Based on published TGA data and the present XRD patterns, this signal is assigned to the decomposition of gypsum (Henning et al., 2023; Lothenbach et al., 2016). Assuming a complete dehydration of gypsum, i.e., formation of anhydrite, the gypsum content can be determined (Fig. 7A). The calculated contents of gypsum might be slightly inaccurate due to the parallel decomposition of C-N-A-S-H and Friedel's salt in the same temperature range. However, in agreement with the XRD results, a strong increase in the gypsum content can be seen after 7 days exposure for C0S4, C5S4 and C14S4. Although the content of gypsum in C0S4 after 7 days of exposure was ~50 % of that in C5S4 and C14S4, the gypsum content after 70 days of exposure was almost identical for the three salt concretes, i.e., no correlation with the Pc content could be identified. Notably, the amounts of gypsum in these concretes after ≥28 days of exposure, referred to the mass of cement paste, were significantly higher than for plain pastes (without salt aggregate) with the same compositions after exposure to the same solution (Henning et al., 2023), and contrary to the latter, continued to significantly increase between 28 and 70 days of exposure.

Although gypsum was also identified in the XRD patterns of salt concrete OPC, its amount in this material was low. Moreover, the TGA/DTG signal of gypsum overlaps with the signals of C-S-H (Lothenbach et al., 2016) and Friedel's salt. Thus, the gypsum content could not be quantified for OPC.

The TGA/DTG signal at ~300 °C, assigned to Friedel's salt for the as-cured salt concretes, shifted to higher temperatures of ~350 °C with increasing periods of exposure for C0S4, C5S4 and C14S4. This shift was delayed with increasing Pc content: the pertinent signal can be found at ~350 °C after 7 days for C0S4, after 28 days for C5S4, and after 56 days for C14S4. This sequence is approximately in agreement with the occurrence of the first indications of Kuzel's salt or a hemicarboaluminate–Friedel's salt solid solution in the XRD patterns of these concretes, and thus the TGA/DTG signal at ~350 °C might be assigned to this secondary AFm phase. In any case, it is evident that the broad signals centered in the range 300–350 °C contained contributions from both Friedel's salt and the secondary AFm phase, and thus these were quantified jointly; henceforth, they will be jointly referred to as Cl-AFm phases. As shown in Fig. 7B, the content of Cl-AFm increased slightly with exposure time for C0S4 and C5S4, while it remained approximately constant for C14S4 and OPC.

3.4. Gas permeability

The gas permeabilities of the as-cured salt concretes and of the concretes after 70 days of exposure to the Q-Tec 4.0 solution were determined to assess their resistance based on the degradation of their microstructure (Table 7). The permeability after curing was in the range 2.3×10^{-15} to 5.3×10^{-15} m^2 for the salt concretes C0S4, C5S4 and C14S4, while it was 3×10^{-17} m^2 for the as-cured OPC salt concrete. Thus, the permeability of the HAC and alkali-activated GGBFS/FA salt concretes was about two orders of magnitude higher than that of the OPC salt concrete.

After 70 days of exposure to the saline solution, the gas permeabilities were increased significantly for all salt concretes. The permeabilities of C0S4, C5S4 and C14S4 were outside the measurement range of the testing device (i.e., higher than 10^{-13} m^2), showing that the microstructure of these concretes had considerably deteriorated during the exposure. The permeability of the OPC salt concrete after exposure was 1×10^{-13} m^2, i.e., it had increased by about four orders of magnitude compared to the as-cured concrete, indicating severe microstructure deterioration during exposure also for this material. However, significant crack formation could not be observed by visual inspection of the specimens, except in the outermost (most severely affected) layers of C0S4 and C5S4 (cf. Fig. 8). Thus, deterioration appears to have been largely restricted to the formation of micro-defects, such as microcracks.

Table 7
Gas permeabilities of the as-cured salt concretes and the concretes after 70 days of exposure to the Q-Tec 4.0 solution.

Exposure time	K(C0S4) (m^2)	K(C5S4) (m^2)	K(C14S4) (m^2)	K(OPC) (m^2)
0 d	5.3×10^{-15}	2.8×10^{-15}	2.3×10^{-15}	3×10^{-17}
70 d	n.d. (>10^{-13})	n.d. (>10^{-13})	n.d. (>10^{-13})	1×10^{-13}

3.5. Deterioration depth

While pH values of the pore solutions of the salt concretes can be assumed to be generally alkaline, lower pH values are expected in areas in which the reactions with the circum-neutral Q-Tec 4.0 solution [$-\log(m_{H+}) \approx 7.9$] have advanced to a large degree. Fig. 8 shows cut surfaces, sprayed with the universal pH indicator solution, of the salt concretes after 7, 28, 56 and 70 days of exposure to the saline solution. A purple color indicates pH ≥ 10 and, thus, areas that can be considered essentially intact, while areas with an orange/yellow color can be expected to be severely corroded.

The penetration of the saline solution into the salt concretes, i.e., the formation and expansion of deteriorated areas, advanced with increasing durations of exposure for C0S4, C5S4 and C14S4. A clear trend towards higher deterioration resistance with increasing Portland clinker content can be observed for these concretes, e.g., a similar size of the remaining intact area was observed for C0S4 after 7 days of exposure, for C5S4 after 28 days, and for C14S4 after 56 days. After 70 days of exposure all salt concretes based on HAC and the alkali-activated GGBFS/FA blend were completely penetrated. However, despite being fully penetrated, the color of the center region of C14S4 indicated that its pH was higher than that of C0S4 and C5S4, i.e., its degree of deterioration was lower, again indicating a higher deterioration resistance of this salt concrete. The images of the OPC salt concrete indicate that it maintained a pH above 10, except for solution penetration to a depth of a few millimeters along its outer surface, for the complete exposure duration up to 70 days, which is in line with the much higher stability of its hydration products, as indicated by XRD and TGA/DTG.

4. Discussion

Comparing the present results with the results for corresponding plain cement pastes with the same composition as those of the salt concretes (Henning et al., 2022, 2023) shows that the addition of the salt aggregate had an important influence on the phase assemblage of the concretes after curing. Instead of ettringite and strätlingite, which were identified in the plain cement pastes, the hydration products in the salt concretes comprised Friedel's salt as main hydration product besides C-N-A-S-H or C-S-H. This is related to the partial dissolution of the salt aggregate during hydration, which increased the concentration of chloride in the pore solution and thus favored the formation of Friedel's salt (Balonis et al., 2010; Birnin-Yauri and Glasser, 1998; Glasser et al., 1999). In addition, the high chloride concentration in the pore solution increases the solubility of portlandite and C-S-H (Galan and Glasser, 2015), and presumably also that of C-N-A-S-H. Accordingly, the formation of the latter phases was delayed in the salt concretes, since more calcium, sodium, aluminum, and silicon have to be dissolved to reach the necessary (super)saturation for their formation. This was likely a reason for the comparatively low early compressive strengths of salt concretes C0S4, C5S4 and C14S4. For the OPC salt concrete, the fast hydration of aluminate to give Friedel's salt in the presence of chloride could have lowered the chloride concentration in the pore solution more rapidly and contributed to its higher early strength. A faster hydration and different phase assemblage of the OPC salt concrete corresponded also to its higher final compressive strength and its considerably lower permeability after curing, compared to the HAC and alkali-activated

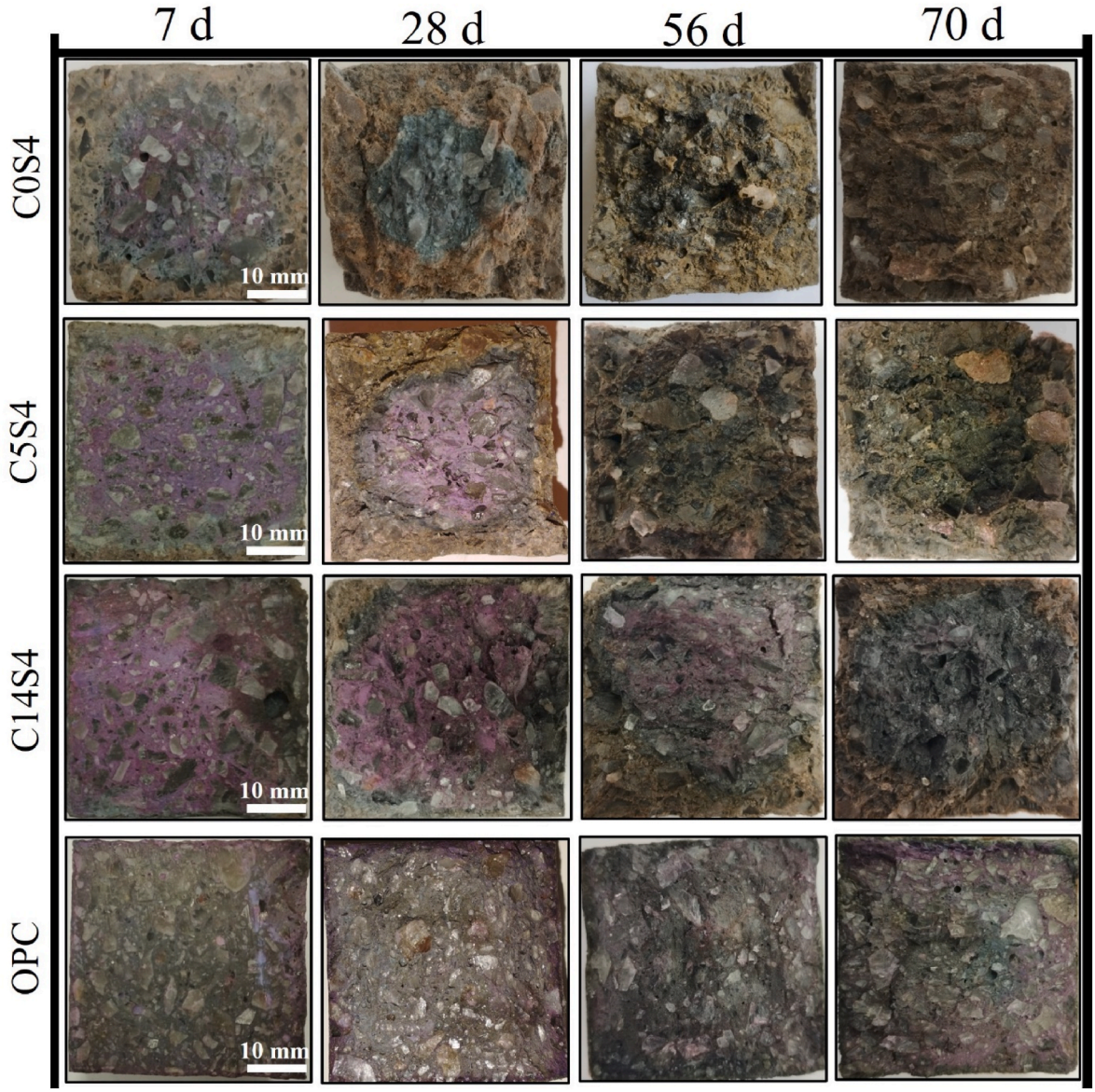

Fig. 8. Images of cut surfaces, sprayed with a universal pH indicator solution (Unisol 410), of the salt concretes C0S4, C5S4, C14S4, and OPC after 7, 28, 56 and 70 days of exposure to the Q-Tec 4.0 solution.

GGBFS/FA salt concretes.

Exposure to the Q-Tec 4.0 solution induced significant changes of the phase assemblages of the salt concretes. Namely, the formation of gypsum and a secondary AFm phase (likely Kuzel's salt or a hemicarboaluminate–Friedel's salt solid solution) was observed, and XRD indicated the partial dissolution of C-N-A-S-H or C-S-H. The formation of gypsum and the secondary AFm phase parallels previous studies, in which these phases were observed after attack of more dilute saline solutions on cementitious materials (De Weerdt et al., 2014; Xue et al., 2021).

Previous studies (Dauzeres et al., 2016; Lerouge et al., 2017) have demonstrated the formation of magnesium silicate hydrate (M-S-H) gel during the deterioration of cementitious materials in Mg-rich environments. It is likely that, in addition to the observed changes of the phase assemblages, this phase had also formed in the salt concretes on exposure to the Q-Tec 4.0 solution, taking up Si that had been released by the dissolution of C-N-A-S-H. M-S-H shares structural characteristics with phyllosilicates such as talc, antigorite or sepiolite; however, it is poorly crystalline or amorphous, its water content is typically much higher than that of the crystalline phyllosilicates, and it has the capacity to swell (Nied et al., 2016; Lerouge et al., 2017; Bernard et al., 2019; Bernard, 2022). Because M-S-H is X-ray amorphous and its main TGA/DTG signal overlaps with that of C-N-A-S-H in the range approx. 50−150 °C (Nied et al., 2016; Bernard et al., 2019), its presence in the deteriorated salt concretes could not be verified in the present study.

In a previous study of plain cement pastes with the same composition as those of the salt concretes, the deterioration of the cement pastes in the circum-neutral Q-Tec 4.0 solution has been conceptualized as a sequence of dissolution and precipitation reactions governed by pH (Henning et al., 2023). In this previous study, the presence of portlandite considerably increased the resistance of the cement pastes against attack by the saline solution, due to its ability to buffer pH at ~12.5. Although the phase assemblages of the cured salt concretes differed from those of the plain pastes, due to the influence of the salt aggregate, similar mechanisms can be assumed to influence the resistance of the concretes. As in the previous study, a higher Portland clinker fraction in the cement pastes led to a better resistance (i.e., lower deterioration depths and later phase transformations), which can be assigned to the ability of portlandite in the OPC salt concrete to buffer pH at ~12.5, and the ability of C-N-A-S-H to buffer pH at ~10. However, an important difference

between the plain cement pastes and the salt concretes was that C14S4 and OPC performed similar in the study of the pastes (Henning et al., 2023), while the resistance of salt concrete C14S4 aligned more with the other HAC salt concrete and was clearly inferior to that of the OPC salt concrete. This can be related to the fact that portlandite was present in the paste C14S4 (likely due to kinetic restrictions during hydration), while it was absent in the salt concrete C14S4. In addition, the considerably higher permeability of the HAC and alkali-activated GGBFS/FA salt concretes, compared to the OPC salt concrete, has clearly contributed to their inferior resistance.

Besides having an influence on the phase assemblage of the salt concretes after curing, the presence of the salt aggregate in the concretes likely had an additional effect on their resistance against attack by the Q-Tec 4.0 solution. For C0S4 and C5S4, XRD indicated a considerable decrease of the amount of anhydrite in the concretes during the first 7 days of exposure, while their gypsum content increased. This suggests that gypsum, in addition to having formed from sulfate in the Q-Tec 4.0 solution and calcium from the dissolution of hydrate phases, had also formed by hydration of the anhydrite impurity in the salt aggregate. This is further indicated by the fact that, at advanced stages of deterioration, the amount of gypsum in the alkali-activated GGBFS/FA and HAC salt concretes (up to ~25 g/100 g cement paste) was about twice the amount of gypsum in the plain cement pastes (<12 g/100 g cement paste; Henning et al., 2023). As a high supersaturation and massive formation of gypsum can lead to the development of crystallization stresses and the associated formation of cracks (Flatt, 2002; Scherer, 2004), the formation of gypsum from anhydrite in the salt aggregate is a likely explanation for the considerable increase of the permeabilities of the salt concretes during exposure to the Q-Tec 4.0 solution.

5. Summary and conclusions

The results of the present study show that the salt aggregate in concretes based on alkali-activated GGBFS/FA blends, hybrid alkaline cements (HAC), and ordinary Portland cement (OPC) has a significant influence on the phase assemblage of the salt concretes and on their resistance against attack by the magnesium chloride-rich Q-Tec 4.0 solution. During curing of the concretes, partial dissolution of halite from the salt aggregate leads to an increased solubility of portlandite, C-S-H and C-N-A-S-H and, thus, delayed early hydration and strength evolution of the alkali-activated GGBFS/FA salt concrete C0S4, and the HAC salt concretes C5S4 and C14S4. Such a delay was not evident for the OPC salt concrete, likely because the latter contains larger quantities of the rapidly reacting clinker phase aluminate, reducing the chloride concentration through formation of Friedel's salt. The different hydration rates and phase assemblages of the concretes led to considerably higher permeabilities of the alkali-activated GGBFS/FA and HAC salt concretes, compared to the OPC salt concrete.

The resistance of the salt concretes against attack by the Q-Tec 4.0 solution increased with increasing Portland clinker fraction in the binder, which is similar to previous observations for plain HAC and OPC pastes (Henning et al., 2023). For the OPC salt concrete, this was related to its low permeability. In addition, the pH-controlled, sequential dissolution of the hydrate phases of the salt concretes in the circum-neutral saline solution played a role for their different resistances. In this dissolution sequence, the portlandite present in OPC buffers the pH in the stability range of C-S-H, while the abundance of the next phase to dissolve, C-N-A-S-H, determines the chemical resistance of the HAC salt concretes.

The deterioration of the main binding phase, C-N-A-S-H, in the HAC salt concretes during exposure to the Q-Tec 4.0 solution parallels observations for salt concretes based on blended cements (Jantschik et al., 2016), and thus indicates that the resistance of HAC salt concretes against attack by magnesium chloride-rich solutions forming in evaporite rock is not fundamentally different from the resistance of salt concretes based on blended cement, i.e., inferior to the resistance of salt concretes based on magnesium oxychloride cement (Jantschik et al., 2016). Thus, the advantage of HAC salt concretes, i.e., their low heat of hydration and the consequently reduced risk of concrete cracking, have to be balanced against their lower chemical resistance for an application in sealing structures in evaporite rock.

An additional mechanism that is likely important for the deterioration of the salt concretes is the formation of gypsum from anhydrite impurities in the salt aggregate. This was deduced from a decrease of the amount of anhydrite in some of the HAC salt concretes and the formation of comparatively high amounts of gypsum. This means that, besides the dissolution of hydrate phases, anhydrite/gypsum-related stress development and cracking of the salt concretes was probably an important reason for the massive increase of their permeabilities during exposure to the Q-Tec 4.0 solution. It is thus apparent that the chemical resistance of salt concretes based on HAC is different from, and more difficult to predict than, the resistance of plain HAC pastes. Spatially resolved analyses at the microstructural level will likely lead to an improved understanding of the relevant mechanisms in future work.

CRediT authorship contribution statement

Ricky Henning: Formal analysis, Investigation, Methodology, Visualization, Writing – original draft. **Patrick Sturm:** Conceptualization, Methodology, Funding acquisition, Project administration, Supervision. **Sylvia Keßler:** Supervision, Writing – review & editing. **Gregor J.G. Gluth:** Conceptualization, Supervision, Writing – review & editing.

Declaration of competing interest

The authors declare that they have no known competing financial interests or personal relationships that could have appeared to influence the work reported in this paper.

Data availability

Data will be made available on request.

Acknowledgements

This study was supported by internal funds within the framework of BAM's MI program [project MIT1-2019-34]. Pia Saborrosch is thanked very much for her diligent support in the laboratory. Helpful conversations about the present study with several participants of the Joint 6th International Workshop on Mechanisms and Modelling of Waste/Cement Interactions (JCCW 2023) and the highly valuable comments and suggestions by the three anonymous reviewers of the initial version of this manuscript are gratefully acknowledged.

References

Altmaier, M., Metz, V., Neck, V., Müller, R., Fanghänel, T., 2003. Solid-liquid equilibria of $Mg(OH)_2$(cr) and $Mg_2(OH)_3Cl{\cdot}4H_2O$(cr) in the system Mg-Na-H-OH-Cl-H_2O at 25°C. Geochem. Cosmochim. Acta 67, 3595–3601. https://doi.org/10.1016/S0016-7037(03)00165-0.

Balonis, M., Lothenbach, B., Le Saout, G., Glasser, F.P., 2010. Impact of chloride on the mineralogy of hydrated Portland cement systems. Cement Concr. Res. 40, 1009–1022. https://doi.org/10.1016/j.cemconres.2010.03.002.

Barbosa, V.F.F., MacKenzie, K.J.D., Thaumaturgo, C., 2000. Synthesis and characterisation of materials based on inorganic polymers of alumina and silica: sodium polysialate polymers. Int. J. Inorg. Mater. 2, 309–317. https://doi.org/10.1016/S1466-6049(00)00041-6.

Bernal, S.A., 2016. Advances in near-neutral salts activation of blast furnace slags. RILEM Tech. Lett. 1, 39–44. https://doi.org/10.21809/rilemtechlett.2016.8.

Bernard, E., 2022. Research progress on magnesium silicate hydrate phases and future opportunities. RILEM Tech. Lett. 7, 47–57. https://doi.org/10.21809/rilemtechlett.2022.162.

Bernard, E., Lothenbach, B., Chlique, C., Wyrzykowski, M., Dauzères, A., Pochard, I., Cau-Dit-Coumes, C., 2019. Characterization of magnesium silicate hydrate (M-S-H). Cement Concr. Res. 116, 309–330. https://doi.org/10.1016/j.cemconres.2018.09.007.

Bette, S., Dinnebier, R.E., Freyer, D., 2017. Impact of a Ni^{2+}-influx on formation, stability, solubility and crystal structures of the magnesia cement phases 3-1-8 and 5-1-8 at 25 °C. J. Environ. Chem. Eng. 5, 5481–5492. https://doi.org/10.1016/j.jece.2017.10.008.

Birnin-Yauri, U.A., Glasser, F.P., 1998. Friedel's salt, $Ca_2Al(OH)_6(Cl,OH)\bullet 2H_2O$: its solid solutions and their role in chloride binding. Cement Concr. Res. 28, 1713–1723. https://doi.org/10.1016/s0008-8846(98)00162-8.

Bracke, G., 2012. Aspects of final disposal of radioactive waste in Germany. Turk. J. Earth Sci. 21, 145–152. https://doi.org/10.3906/yer-1006-18.

Cau Dit Coumes, C., Courtois, S., Nectoux, D., Leclercp, S., Bourbon, X., 2006. Formulating a low-alkalinity, high-resistance and low-heat concrete for radioactive waste repositories. Cement Concr. Res. 36, 2152–2163. https://doi.org/10.1016/j.cemconres.2006.10.005.

Codina, M., Cau-dit-Coumes, C., Le Bescop, P., Verdier, J., Ollivier, J.P., 2008. Design and characterization of low-heat and low-alkalinity cements. Cement Concr. Res. 38, 437–448. https://doi.org/10.1016/j.cemconres.2007.12.002.

Collier, N.C., Sharp, J.H., Milestone, N.B., Hill, J., Godfrey, I.H., 2008. The influence of water removal techniques on the composition and microstructure of hardened cement pastes. Cement Concr. Res. 38, 737–744. https://doi.org/10.1016/j.cemconres.2008.02.012.

Dauzeres, A., Achiedo, G., Nied, D., Bernard, E., Alahrache, S., Lothenbach, B., 2016. Magnesium perturbation in low-pH concretes placed in clayey environment—solid characerizations and modeling. Cement Concr. Res. 79, 137–150. https://doi.org/10.1016/j.cemconres.2015.09.002.

DBE, 2004a. Verfüllmaterial für Strecken mit hohen Anforderungen: Materialeigenschaften und Materialkennwerte Salzbeton M2. Unterlage P 192. Bundesamt für Strahlenschutz (BfS), Salzgitter.

DBE, 2004b. Verfüllmaterial für Strecken mit hohen Anforderungen: Konzeptplanung und Nachweisführung. Unterlage P 195, Teil 1 von 2. Bundesamt für Strahlenschutz (BfS), Salzgitter.

DBE, 2009. Anforderungen an Salzbeton als Baustoff für Abdichtbauwerke im Steinsalz. Unterlage G 296. Bundesamt für Strahlenschutz (BfS), Salzgitter.

De Weerdt, K., Justnes, H., Geiker, M.R., 2014. Changes in the phase assemblage of concrete exposed to sea water. Cem. Concr. Compos. 47, 53–63. https://doi.org/10.1016/j.cemconcomp.2013.09.015.

Dinnebier, R.E., Freyer, D., Bette, S., Oestreich, M., 2010. $9Mg(OH)_2\bullet MgCl_2\bullet 4H_2O$, a high temperature phase of the magnesia binder system. Inorg. Chem. 49, 9770–9776. https://doi.org/10.1021/ic1004566.

Donatello, S., Fernández-Jimenez, A., Palomo, A., 2013. Very high volume fly ash cements. Early age hydration study using Na_2SO_4 as an activator. J. Am. Ceram. Soc. 96, 900–906. https://doi.org/10.1111/jace.12178.

Duxson, P., Provis, J.L., Lukey, G.C., Separovic, F., van Deventer, J.S.J., 2005. ^{29}Si NMR study of structural ordering in aluminosilicate geopolymer gels. Langmuir 21, 3028–3036. https://doi.org/10.1021/la047336x.

Etcheverry, J.M., Yue, Z., Krishnan, S., Villagran-Zaccardi, Y.A., Van den Heede, P., Dhandapani, Y., Bernal, S.A., De Belie, N., 2023. Phase evolution of hybrid alkali sulfate-activated ground-granulated blast furnace slag cements. ACS Sustain. Chem. Eng. 11, 17519–17531. https://doi.org/10.1021/acssuschemeng.3c05937.

Flatt, R.J., 2002. Salt damage in porous materials: how high supersaturations are generated. J. Cryst. Growth 242, 435–454. https://doi.org/10.1016/S0022-0248(02)01429-X.

Fletcher, R.A., MacKenzie, K.J.D., Nicholson, C.L., Shimada, S., 2005. The composition range of aluminosilicate geopolymers. J. Eur. Ceram. Soc. 25, 1471–1477. https://doi.org/10.1016/j.jeurceramsoc.2004.06.001.

Galan, I., Glasser, F.P., 2015. Chloride in cement. Adv. Cement Res. 27, 63–97. https://doi.org/10.1680/adcr.13.00067.

García-Lodeiro, I., Fernández-Jiménez, A., Palomo, A., 2013. Variation in hybrid cements over time. Alkaline activation of fly ash–portland cement blends. Cement Concr. Res. 52, 112–122. https://doi.org/10.1016/j.cemconres.2013.03.022.

Garcia-Lodeiro, I., Donatello, S., Fernández-Jiménez, A., Palomo, A., 2016. Hydration of hybrid alkaline cement containing a very large proportion of fly ash: a descriptive model. Materials 9, 605. https://doi.org/10.3390/ma9070605.

Georget, F., Lothenbach, B., Wilson, W., Zunino, F., Scrivener, K.L., 2022. Stability of hemicarbonate under cement paste-like conditions. Cement Concr. Res. 154, 106692 https://doi.org/10.1016/j.cemconres.2021.106692.

Glasser, F.P., Kindness, A., Stronach, S.A., 1999. Stability and solubility relationships in AFm phases: Part I. Chloride, sulfate and hydroxide. Cement Concr. Res. 29, 861–866. https://doi.org/10.1016/s0008-8846(99)00055-1.

Gluth, G.J.G., Garel, S., 2021. Calorimetry study of the influence of Portland cement content, slag/fly ash ratio, and activator type on the early hydration of hybrid cements. In: Valente, I.B., Ventura Gouveia, A., Dias, S.S. (Eds.), Proceedings of the 3rd RILEM Spring Convention and Conference (RSCC 2020) – Volume 2: New Materials and Structures for Ultra-durability. RILEM Bookseries, vol. 33. Springer, Cham, pp. 217–226. https://doi.org/10.1007/978-3-030-76551-4_20.

Greiser, S., Gluth, G.J.G., Sturm, P., Jäger, C., 2018. $^{29}Si\{^{27}Al\}$, $^{27}Al\{^{29}Si\}$ and $^{27}Al\{^{1}H\}$ double-resonance NMR spectroscopy study of cementitious sodium aluminosilicate gels (geopolymers) and gel–zeolite composites. RSC Adv. 8, 40164–40171. https://doi.org/10.1039/c8ra09246j.

Henning, R., Sturm, P., Geddes, D.A., Keßler, S., Walkley, B., Gluth, G.J.G., 2022. The influence of curing temperature on the strength and phase assemblage of hybrid cements based on GGBFS/FA blends. Front. Mater. 9, 982568 https://doi.org/10.3389/fmats.2022.982568.

Henning, R., Sturm, P., Keßler, S., Gluth, G.J.G., 2023. Corrosion of hybrid alkaline cements in saline solution simulating evaporite rock – effect of the Portland clinker content. Cement Concr. Res. 172, 107215 https://doi.org/10.1016/j.cemconres.2023.107215.

Jackson, M.D., Chae, S.R., Mulcahy, S.R., Meral, C., Taylor, R., Li, P., Emwas, A.-H., Moon, J., Yoon, S., Vola, G., Wenk, H.-R., Monteiro, P.J.M., 2013a. Unlocking the secrets of Al-tobermorite in Roman seawater concrete. Am. Mineral. 98, 1669–1687. https://doi.org/10.2138/am.2013.4484.

Jackson, M.D., Moon, J., Gotti, E., Taylor, R., Chae, S.R., Kunz, M., Emwas, A.-H., Meral, C., Guttmann, P., Levitz, P., Wenk, H.-R., Monteiro, P.J.M., 2013b. Material and elastic properties of Al-tobermorite in ancient Roman seawater concrete. J. Am. Ceram. Soc. 96, 2598–2606. https://doi.org/10.1111/jace.12407.

Jackson, M.D., Mulcahy, S.R., Chen, H., Li, Y., Li, Q., Cappelletti, P., Wenk, H.-R., 2017. Phillipsite and Al-tobermorite mineral cements produced through low-temperature water-rock reactions in Roman marine concrete. Am. Mineral. 102, 1435–1450. https://doi.org/10.2138/am-2017-5993CCBY.

Jantschik, K., Czaikowski, O., Moog, H.C., Wieczorek, K., 2016. Investigating the sealing capacity of a seal system in rock salt (DOPAS project). Kerntechnik 81, 571–585. https://doi.org/10.3139/124.110721.

Jantschik, K., Czaikowski, O., Hertes, U., Meyer, T., Moog, H.C., Zehle, B., 2018. Development of Chemical-Hydraulic Models for the Prediction of Long-Term Sealing Capacity of Concrete-Based Sealing Materials in Rock Salt. Gesellschaft für Anlagen- und Reaktorsicherheit (GRS), Köln.

Krupp, R.E., 2005. Formation and chemical evolution of magnesium chloride brines by evaporite dissolution processes—implications for evaporite geochemistry. Geochem. Cosmochim. Acta 69, 4283–4299. https://doi.org/10.1016/j.gca.2004.11.018.

Kulik, D.A., 2011. Improving the structural consistency of C-S-H solid solution thermodynamic models. Cement Concr. Res. 41, 477–495. https://doi.org/10.1016/j.cemconres.2011.01.012.

Lerouge, C., Gaboreau, S., Grangeon, S., Claret, F., Warmont, F., Jenni, A., Cloet, V., Mäder, U., 2017. In situ interactions between opalinus clay and low alkali concrete. Phys. Chem. Earth 99, 3–21. https://doi.org/10.1016/j.pce.2017.01.005.

Lothenbach, B., Nonat, A., 2015. Calcium silicate hydrates: solid and liquid phase composition. Cement Concr. Res. 78, 57–70. https://doi.org/10.1016/j.cemconres.2015.03.019.

Lothenbach, B., Le Saout, G., Ben Haha, M., Figi, R., Wieland, E., 2012. Hydration of a low-alkali CEM III/B–SiO_2 cement (LAC). Cement Concr. Res. 42, 410–423. https://doi.org/10.1016/j.cemconres.2011.11.008.

Lothenbach, B., Durdziński, P., De Weerdt, K., 2016. Thermogravimetric analysis. In: Scrivener, K., Snellings, R., Lothenbach, B. (Eds.), A Practical Guide to Microstructural Analysis of Cementitious Materials. CRC Press, Boca Raton, pp. 177–211.

Mengel, K., Röhlig, K.-J., Geckeis, H., 2012. Endlagerung radioaktiver abfälle: die wirtsgesteine: tonstein, granit, steinsalz. Chem. Unserer Zeit 46, 208–217. https://doi.org/10.1002/ciuz.201200582.

Myers, R.J., Bernal, S.A., San Nicolas, R., Provis, J.L., 2013. Generalized structural description of calcium–sodium aluminosilicate hydrate gels: the cross-linked substituted tobermorite model. Langmuir 29, 5294–5306. https://doi.org/10.1021/la4000473.

Myers, R.J., Bernal, S.A., Provis, J.L., 2014. A thermodynamic model for C-(N-)A-S-H gel: CNASH_ss. Derivation and validation. Cement Concr. Res. 66, 27–47. https://doi.org/10.1016/j.cemconres.2014.07.005.

Myers, R.J., L'Hôpital, E., Provis, J.L., Lothenbach, B., 2015. Composition–solubility–structure relationships in calcium (alkali) aluminosilicate hydrate (C-(N,K-)A-S-H). Dalton Trans. 44, 13530–13544. https://doi.org/10.1039/c5dt01124h.

Myers, R.J., Bernal, S.A., Provis, J.L., 2017. Phase diagrams for alkali-activated slag binders. Cement Concr. Res. 95, 30–38. https://doi.org/10.1016/j.cemconres.2017.02.006.

Nath, P., Sarker, P.K., 2015. Use of OPC to improve setting and early strength properties of low calcium fly ash geopolymer concrete cured at room temperature. Cem. Conr. Compos. 55, 205–214. https://doi.org/10.1016/j.cemconcomp.2014.08.008.

Nied, D., Enemark-Rasmussen, K., L'Hopital, E., Skibsted, J., Lothenbach, B., 2016. Properties of magnesium silicate hydrates (M-S-H). Cement Concr. Res. 79, 323–332. https://doi.org/10.1016/j.cemconres.2015.10.003.

Palomo, A., Alonso, S., Fernandez-Jiménez, A., Sobrados, I., Sanz, J., 2004. Alkaline activation of fly ashes: NMR study of the reaction products. J. Am. Ceram. Soc. 87, 1141–1145. https://doi.org/10.1111/j.1551-2916.2004.01141.x.

Palomo, A., Monteiro, P., Martauz, P., Bilek, V., Fernandez-Jimenez, A., 2019. Hybrid binders: a journey from the past to a sustainable future (*opus caementicium futurum*). Cement Concr. Res. 124, 105829 https://doi.org/10.1016/j.cemconres.2019.105829.

Park, S., Moges, K.A., Wu, S., Pyo, S., 2022. Characteristics of hybrid alkaline cement composites with high cement content: flash set and high compressive strength. J. Mater. Res. Technol. 17, 1582–1597. https://doi.org/10.1016/j.jmrt.2022.01.105.

Puertas, F., Palacios, M., Manzano, H., Dolado, J.S., Rico, A., Rodríguez, J., 2011. A model for the C-A-S-H gel formed in alkali-activated slag cements. J. Eur. Ceram. Soc. 31, 2043–2056. https://doi.org/10.1016/j.jeurceramsoc.2011.04.036.

Richardson, I.G., 1999. The nature of C-S-H in hardened cements. Cement Concr. Res. 29, 1131–1147. https://doi.org/10.1016/S0008-8846(99)00168-4.

Richardson, I.G., 2004. Tobermorite/jennite- and tobermorite/calcium hydroxide-based models for the structure of C-S-H: applicability to hardened pastes of tricalcium silicate, β-dicalcium silicate, Portland cement, and blends of Portland cement with blast-furnace slag, metakaolin, or silica fume. Cement Concr. Res. 34, 1733–1777. https://doi.org/10.1016/j.cemconres.2004.05.034.

Richardson, I.G., 2014. Model structures for C-(A)-S-H(I). Acta Crystallogr. B 70, 903–923. https://doi.org/10.1107/S2052520614021982.

RILEM TC 116-PCD, 1999. Tests for gas permeability of concrete: B. Measurement of the gas permeability of concrete by the RILEM-Cembureau method. Mater. Struct. 32, 176–178. https://doi.org/10.1007/BF02481511.

Scherer, G.W., 2004. Stress from crystallization of salt. Cement Concr. Res. 34, 1613–1624. https://doi.org/10.1016/j.cemconres.2003.12.034.

Thiery, M., Villain, G., Dangla, P., Platret, G., 2007. Investigation of the carbonation front shape on cementitious materials: effects of chemical kinetics. Cement Concr. Res. 37, 1047–1058. https://doi.org/10.1016/j.cemconres.2007.04.002.

Taylor, H.F.W., 1997. Cement Chemistry, second ed. Thomas Telford, London.

Walkley, B., Rees, G.J., San Nicolas, R., van Deventer, J.S.J., Hanna, J.V., Provis, J.L., 2018. New structural model of hydrous sodium aluminosilicate gels and the role of charge-balancing extra-framework Al. J. Phys. Chem. C 122, 5673–5685. https://doi.org/10.1021/acs.jpcc.8b00259.

Wilson, W., Gonthier, J.N., Georget, F., Scrivener, K.L., 2022. Insights on chemical and physical chloride binding in blended cement pastes. Cement Concr. Res. 156, 106747 https://doi.org/10.1016/j.cemconres.2022.106747.

Xue, L., Zhang, Z., Wang, H., 2021. Hydration mechanisms and durability of hybrid alkaline cements (HACs): a review. Construct. Build. Mater. 266, 121039 https://doi.org/10.1016/j.conbuildmat.2020.121039.